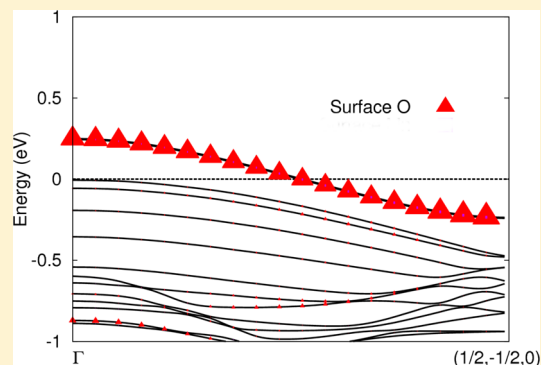


# Surfaces of Rutile $\text{MnO}_2$ Are Electronically Conducting, Whereas the Bulk Material Is Insulating

David A. Tompsett\* and M. Saiful Islam\*

Department of Chemistry, University of Bath, Bath BA2 7AY, U.K.

**ABSTRACT:** The nanostructuring of rutile  $\text{MnO}_2$  has been demonstrated to improve its performance for electrochemical storage and catalysis. Despite the progress of recent experimental works in exploiting this to enhance the material's performance in important technological systems such as Li-ion batteries the detailed atomic-scale mechanisms still require explanation. The ability of surfaces and interfaces to produce intriguing phenomena including superconductivity and magnetism has been firmly established by intensive research in recent years. In this work we use density functional theory calculations to demonstrate that key surfaces of rutile  $\text{MnO}_2$  possess electronically conducting surface states, in contrast to the insulating bulk material. The surface band structure demonstrates that the conducting states are associated with both surface manganese and oxygen sites. Furthermore, the metallic conductivity is found to be anisotropic for the (001) surface, which may be exploited in device applications. The implications for the energy storage capacity and catalytic activity of rutile  $\text{MnO}_2$  are discussed in light of the need for good electron transport in Li-ion batteries, supercapacitors, and Li– $\text{O}_2$  batteries.



## INTRODUCTION

Surfaces and interfaces have the ability to produce novel behavior that is distinct from the associated bulk materials. For instance, bulk insulators and semiconductors may possess metallic surfaces.<sup>1,2</sup> Furthermore, the interface between two insulating nonmagnetic oxides,  $\text{LaAlO}_3$  and  $\text{SrTiO}_3$ , exhibits superconductivity and magnetism.<sup>3</sup> The inherent fundamental interest in these systems is matched by the potential for technological exploitation of the diverse array of electronic and crystal properties that may be achieved by surface and interface engineering. In this work, we investigate the electronic properties at the surfaces of the promising electrode and catalyst rutile  $\text{MnO}_2$  using first-principles simulations. The results indicate the tendency to form metallic conductivity at important surfaces. This behavior is distinct from the insulating bulk crystal structure and may be important to the good performance of rutile  $\text{MnO}_2$  as a catalyst and as an electrochemical electrode.

Energy storage for hybrid electric vehicles and renewable energy sources is a pressing technological challenge. Rutile  $\text{MnO}_2$  has been the subject of intense investigations in energy storage systems based on Li-ion batteries,<sup>4–8</sup> supercapacitors,<sup>9–12</sup> and the topical Li– $\text{O}_2$  battery system.<sup>13,14</sup> By their electrochemical nature all of these systems require efficient transport of electrons, and therefore the development of materials with enhanced electron conductivity is desirable.

In Li-ion batteries electrons flow around an external circuit during discharge and then must be transported through the cathode to the redox active sites. Since many high-capacity cathodes discovered to date are poor electronic conductors<sup>15–18</sup> their intrinsic electron transport requires improve-

ment in practical cells. Consequently, battery designs typically incorporate carbon loading to enhance conductivity between and around electrode particles,<sup>19–21</sup> but this also increases the electrode mass. For this reason the ability to produce metallic states, or states with improved conductivity, at oxide electrode surfaces is of practical interest to the battery research community. The ability to incorporate such phenomena into battery materials has the potential to both increase rate performance and enhance the energy density, which are chief metrics of electrode performance.

When employed as a Li-ion battery cathode nanostructured rutile  $\text{MnO}_2$  has also been demonstrated to possess significantly enhanced capacity<sup>4,5,7,8</sup> compared to bulk samples, which have been shown to not permit significant Li intercalation.<sup>4,22,23</sup> Recent first-principles work has suggested that nanostructuring improves the kinetics for Li-ions to move from the surface into the material bulk.<sup>24</sup> However, surfaces may also affect the supply of electrons which are essential to the redox reaction that underpins the energy storage of Li-ion batteries. The transport of electrons at key surfaces of rutile  $\text{MnO}_2$  is addressed in the present work.

In the context of electrochemical electrodes, rutile  $\text{MnO}_2$  has attracted particularly strong attention in nanostructured form since the storage capacity is directly related to the material surface area. Initial work utilizing bulk rutile  $\text{MnO}_2$  crystallites as supercapacitor electrodes<sup>11</sup> showed a low capacity of  $\sim 9 \text{ F g}^{-1}$ . However, nanostructured electrodes exhibited improved

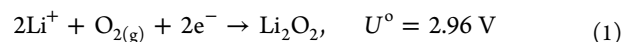
Received: July 18, 2014

Revised: September 30, 2014

Published: September 30, 2014

capacitance of 294 F g<sup>-1</sup>.<sup>12</sup> In supercapacitors a chief mechanism of the energy storage is derived from the presence of an electric double layer, which forms at the interface between the electrode and the liquid electrolyte. The double layer refers to the two oppositely charged layers that form. One layer is formed by charged ions adsorbing from the electrolyte onto the electrode surface. The second oppositely charged layer forms on the inner side of the electrode due to either accumulation or depletion of electrons. Clearly the formation of this second layer may benefit from enhanced electron mobility in the electrode. Consequently, the surface electronic structure of rutile MnO<sub>2</sub> is important to its performance as a supercapacitor electrode.

Rutile MnO<sub>2</sub> has demonstrated good performance as a catalyst for the oxygen reduction reaction in alkaline fuel cells,<sup>25</sup> oxidation of Cr<sup>III</sup> to Cr<sup>VI</sup>,<sup>26,27</sup> oxidation of toxic As<sup>III</sup> to As<sup>V</sup>,<sup>28,29</sup> and water electrolysis.<sup>30</sup> In the context of energy materials rutile MnO<sub>2</sub> has received attention due to its promising performance in catalyzing reactions in the Li–O<sub>2</sub> battery.<sup>13,14</sup> Although recent work has suggested the presence of electrolyte decomposition in earlier reports<sup>31–34</sup> it is likely that the utility of catalysts will be the subject of future studies.<sup>35,36</sup> In the absence of solvent degradation the Li–O<sub>2</sub> cell is based upon the following reaction:



A supply of both oxygen and electrons is required for the oxidation of Li-ions to proceed. In previous work<sup>37</sup> low formation energies for oxygen vacancy formation at rutile MnO<sub>2</sub> surfaces were demonstrated. The formation of vacancies may be a key step in supplying oxygen for this reaction. In this work we investigate the potential to transport electrons to reaction sites at rutile MnO<sub>2</sub> surfaces.

Nanostructuring has been shown to improve the energy storage properties of rutile MnO<sub>2</sub> for both Li-ion batteries and supercapacitors,<sup>9,10,38</sup> and its efficacy as a catalyst.<sup>13</sup> With nanostructuring the proportion of the material that lies at or near the surface increases. Indeed, the increased role of surface properties may be critical to the improved performance brought about by nanostructuring.<sup>39</sup>

The ability to produce metallic surfaces has been discussed for spin injection in spintronic devices. However, the typical doping required to produce metallicity in the semiconducting materials increases scattering to the detriment of device performance.<sup>40</sup> The ability to engineer surfaces to produce intrinsic surface metallicity, such as observed in the present work, has the potential to circumvent these problems.

Pristine rutile MnO<sub>2</sub> occurs in the tetragonal space group *P4/mmm* (No. 136)<sup>41,42</sup> as shown in Figure 1a. The dominant structural building block is the MnO<sub>6</sub> octahedra that are edge-sharing along the *c*-axis and corner sharing in the plane. Alongside in Figure 1b the equilibrium morphology from a recent density functional theory (DFT) investigation<sup>37</sup> is shown. The elongation of this morphology is consistent with the large number of needle-like nanostructures that have been observed to form during experimental synthesis.<sup>7,8,13,14</sup> In the present work we are chiefly concerned with the intriguing properties at the expressed surfaces, in particular with the labeled (110) and (001) surface planes. A detailed understanding of the atomic-scale and electronic properties of these surfaces is essential to understanding their important role in electrochemistry and catalysis.

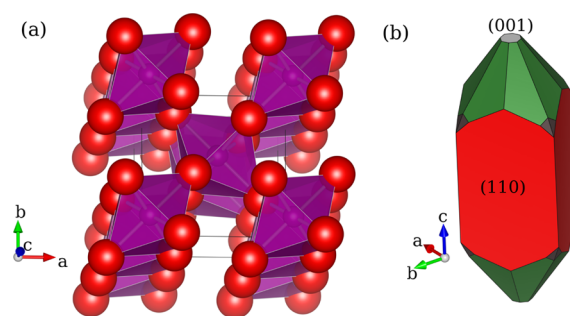


**Figure 1.** Diagram of (a) the crystal structure of  $\beta$ -MnO<sub>2</sub>. Large (red) spheres are oxygen and small (purple) manganese lie inside the indicated approximate MnO<sub>6</sub> octahedra. Note the tunnel structure along the *c*-axis. Panel b depicts the equilibrium crystal morphology predicted by a recent DFT investigation.<sup>37</sup>

The potential importance of rutile MnO<sub>2</sub> in energy storage and catalytic applications has provided a strong impetus to study its surfaces experimentally. An early investigation of manganese oxide surfaces, including rutile MnO<sub>2</sub>, applied X-ray photoelectron spectroscopy (XPS).<sup>43</sup> It found evidence for the surface reduction of rutile above 400 °C, but did not characterize the surface structure. More recently, electron energy loss spectroscopy (EELS) has been applied to the naturally occurring mineral form of rutile MnO<sub>2</sub>, pyrolusite. The average valence of the surface was found to be +4.0, in agreement with the formal valence. Growth of thin films of rutile MnO<sub>2</sub> on the surfaces of other oxides has been investigated. Chambers and Liang<sup>44</sup> used reflection high-energy electron diffraction to demonstrate the growth of up to six bilayers of rutile MnO<sub>2</sub> on the rutile TiO<sub>2</sub> (110) surface. Rutile MnO<sub>2</sub> films have also been grown by Xing et al.<sup>45</sup> on the (001) surface of both LaAlO<sub>3</sub> and MgO. In that work the presence of some reduced Mn<sup>3+</sup> was observed by XPS. We will return to discuss these observations in light of our findings.

In addition to this experimental work our understanding of MnO<sub>2</sub> has also been aided by computational studies.<sup>18,46–49</sup> Maphanga et al.<sup>46</sup> applied interatomic force field methods to characterize low index surfaces of rutile MnO<sub>2</sub>. Oxford and Chaka<sup>47</sup> applied the Generalized Gradient Approximation (GGA) in density functional theory (DFT) to consider the low index surfaces (110), (100), and (101) of rutile MnO<sub>2</sub>. They calculated the surface energies of stoichiometric as well as heavily oxidized and reduced surfaces. Their results indicated that the stoichiometric surfaces were the most stable at experimentally accessible conditions. In recent work the present authors and others have considered the surface energies up to high Miller index and predicted an elongated morphology that is consistent with the large number of nanostructures observed experimentally.<sup>37</sup> That work also demonstrated low formation energies for oxygen vacancies at rutile MnO<sub>2</sub> surfaces, which are likely to be important to its good catalytic performance. This study extends the analysis of important surfaces to consider the electronic conductivity.

## ■ COMPUTATIONAL METHODS

The electronic structure of important surfaces was treated by DFT as implemented in the VASP code.<sup>50</sup> The electronic structure was calculated using the Generalized Gradient Approximation of Perdew–Burke–Ernzerhof<sup>51</sup> with Hubbard *U* corrections (GGA+*U*). PAW potentials were employed and the cutoff for the planewave basis set was 400 eV. A minimum

of  $4 \times 4 \times 4$   $k$ -points was used in the Brillouin zone of the conventional cell for structural relaxation and  $10 \times 10 \times 10$  for calculation of the density of states (DOS). These  $k$ -point grids were scaled appropriately for surface slabs.

The value of the  $U$  parameter for our GGA+ $U$  calculations was determined ab initio using Wien2k<sup>52–54</sup> in a previous work conducted by the present authors.<sup>18,39</sup> Those studies demonstrated a good description of lithium intercalation, band gaps, and magnetic interactions, and we use the same values of  $U$  here. We employ  $(U - J) = 5.1$  eV, for the spherical part of the interaction for the remainder of this study. Since the exchange interaction is poorly screened in solids<sup>55,56</sup> we employ an atomic limit value  $J = 1.0$  eV and the fully localized limit double counting correction.<sup>57</sup> All calculations were performed in a ferromagnetic spin configuration.

The relaxed bulk geometry was used to construct surfaces with slab geometries for the calculation of *ab initio* surface energies using VASP. For the relaxation of the bulk unit cell a higher planewave cutoff of 520 eV was employed to avoid errors due to Pulay stress. Surface energies are calculated on the basis of slabs with a minimum thickness of 15 Å, where for each surface the slab thickness is increased until convergence of the surface energy is obtained. A vacuum thickness greater than 20 Å was used throughout to separate the slabs from their periodic image. All slabs were constructed to possess symmetric top and bottom surfaces. Full geometrical relaxation of the ionic positions until the forces fell below  $0.02 \text{ eV \AA}^{-1}$  was performed to incorporate surface relaxation effects.

## SURFACE ELECTRONIC STRUCTURE

The catalytic activity of  $\text{MnO}_2$  in  $\text{Li-O}_2$  batteries, water electrolysis, and other applications is likely to be driven by processes that enhance the availability of both ions and electrons to participate in reactions. The reaction for the formation of lithium peroxide in eq 1 requires the delivery of two electrons to the reaction site. The first step in electrolysis in alkaline media involves the removal of an electron via the step  $(\text{OH})^- \rightarrow (\text{OH}) + e^-$ . Here, we evaluate the ability of surfaces expressed in the equilibrium morphology of rutile  $\text{MnO}_2$  to deliver these electrons by probing the electronic conductivity at these surfaces.

Figure 2 panels a and b show the electronic density of states (DOS) arising from slabs constructed for two prominent surfaces expressed in the equilibrium morphology, the low index (110) and (001) surfaces. While the bulk electronic

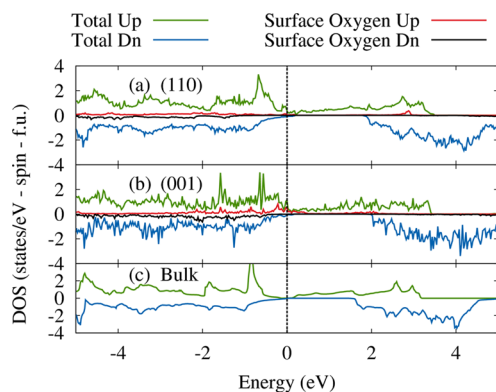


**Figure 2.** Density of states for energetically preferred surface slabs of  $\beta\text{-MnO}_2$ , (a) (110) and (b) (001) in comparison to (c) bulk.

structure in Figure 2c is gapped,<sup>18</sup> it is clear that both the (110) and (001) surfaces possess metallic states at the Fermi level. The presence of metallic states is identified by a finite DOS at the Fermi level, while for a nonmetallic system the DOS should fall to exactly zero. Together the (110) and (001) surfaces represent 65% of the crystal morphology and consequently these metallic states may provide electrons to a large effective area of the surface catalytic sites.

We note that the higher index (211) and (311) surfaces, which are also expressed in the equilibrium morphology, retain a small gap in their DOS of approximately 0.2 eV. This finding presents the potential to optimize the surface electronic conductivity by synthesizing crystals under conditions that express desirable surfaces. The value of the calculated gap for bulk rutile  $\text{MnO}_2$  is considerably smaller than the isostructural rutile  $\text{TiO}_2$ ,<sup>58</sup> which possesses a gap of 3 eV in the bulk and is found to possess no metallic states at the stoichiometric (110) surface.<sup>59</sup>

We now return to consider the mechanism that gives rise to the metallic states of the (110) and (001) surfaces. Figure 3

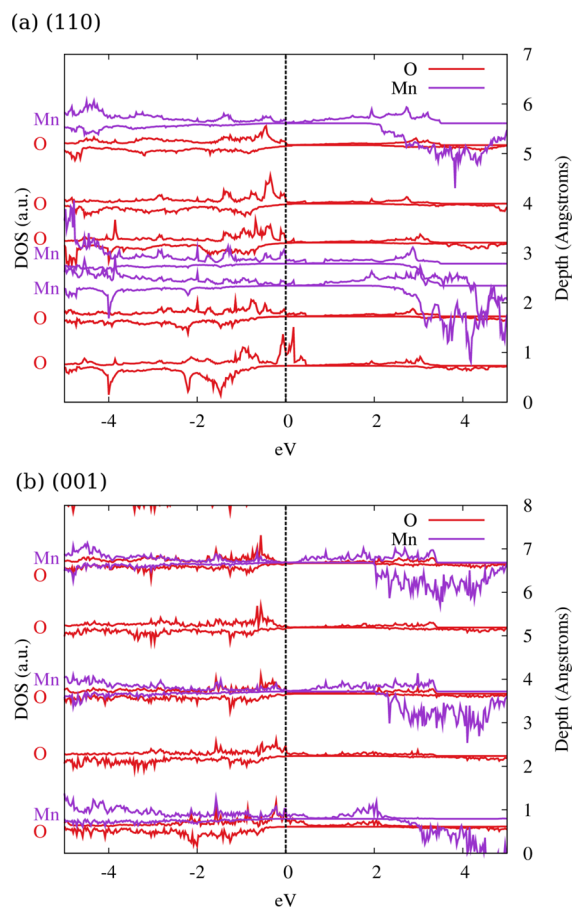


**Figure 3.** Site projected DOS for atoms in the near surface layers of (a) the (110) and (b) (001) surface.

shows the site projected DOS for the near surface layers of the (110) and (001) surface. The depth of the site relative to the outer surface layer is indicated on the right-hand axis. From Figure 3a it is clear that the primary contribution to the metallic states for (110) arises due to a strongly spin polarized contribution from the oxygen site in the outer surface layer. There is also a smaller contribution from an oxygen site at a depth of approximately 1.75 Å and from two manganese sites

between 2 and 3 Å from the surface. Deeper layers are gapped in a manner that is consistent with bulk-like electronic structure. The presence of contributions to the metallic surface states from spin polarized oxygen sites is consistent with a recent work by Radin et al.<sup>60</sup> on  $\text{Li}_2\text{O}_2$ .

For the (001) surface in Figure 3b the strongest contribution to the finite DOS at the Fermi level, that is the hallmark of metallic character, is due to O and Mn in the outermost surface layer. As we inspect the DOS for layers deeper toward the bulk a clear gap quickly re-emerges. The important contribution of surface sites, for both (110) and (001), emphasizes the strong connection between the broken coordination due to cleaving the surface plane and the resultant metallic states. Indeed a Bader charge analysis at the (110) surface demonstrates that the surface oxygen sites that contribute to the metallicity also possess a decreased Bader charge of approximately 6.7 electrons compared to 7.1 in the bulk. Therefore, these surface sites indicate a tendency to behave more like an  $\text{O}^-$  hole species and therefore may be important to catalytic reactivity.

The experimental observation of Mn valence states below the formal valence of  $\text{Mn}^{4+}$  for rutile  $\text{MnO}_2$  has typically been attributed to the presence of oxygen vacancies.<sup>43,45</sup> However, the presence of metallic states may also play a role by reducing the ionicity of Mn sites, as evidenced by the Bader charge discussion above, and therefore permitting deviation from the formal valence. Metallic states at the surfaces of other insulating oxides including  $\text{Li}_2\text{O}_2$  have recently been observed.<sup>60</sup> The presence of averaged Mn oxidation states below 3.5 at manganese oxide surfaces has also been observed by XPS for spinel-type structures.<sup>61</sup>

Inspection of the orbitally projected site DOS indicates that the metallic states are due to a  $p_z$  orbital. These orbitals run along the plane of the crystal surface in the  $[1\bar{1}0]$  direction as shown for the (110) surface in Figure 4a. Similarly for the (001) surface, p-orbitals in near surface layers provide the main contribution to the metallic conductivity. For this surface the involved p-orbitals are oriented along the surface with their axis also pointing in the  $[1\bar{1}0]$  direction as shown in Figure 4b. These directions are given with respect to the axes of the bulk

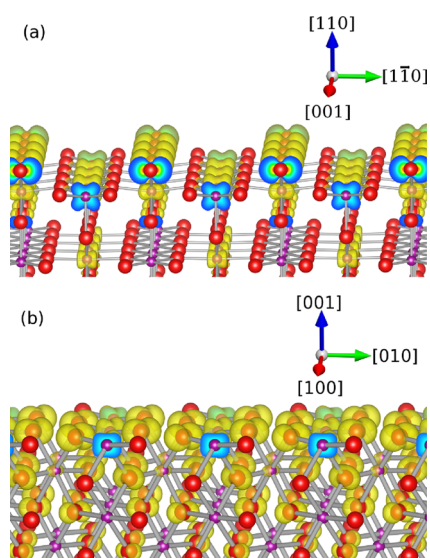


**Figure 4.** Charge density associated with metallic surface states at the (a) (110) and (b) (001) surfaces. Obtained by projecting the charge density for an energy range  $\pm 0.1$  eV either side of the Fermi level.

cell. Therefore, the metallic surface states at these two surfaces, though having different terminations after cleaving, are actually associated with p-orbitals which are oriented in the same direction with respect to the bulk material. The large contribution of the surface oxygen sites to the metallic states as shown in Figure 3 suggests that ease of electron hopping between oxygen sites is likely to be at play. The potential for surface reconstructions to impact this mechanism warrants further investigation.

We may further probe the properties of the conducting surface states by plotting the wavevector dependent bandstructure. The wavevector dependent bandstructure simply shows the energy eigenvalue associated with electrons as a function of their crystal momentum in the lattice. The bandstructure for the (110) surface slab is plotted in Figure 5 for the set of wavevectors aligned with the  $[1\bar{1}0]$  direction associated with the surface p-orbitals. It is clear that for both the spin up states in Figure 5a and the down states in Figure 5b there exists a dispersion line that crosses the Fermi level. It is the states near to the Fermi level crossing points that are important to the metallic properties of this surface. To probe the nature of these states we overlaid the atomic character associated with these states. It is very clear that in Figure 5a the spin up metallic states are dominated by surface Mn sites (c.f. large purple character of the band crossing the Fermi level). Furthermore, the spin down channel (Figure 5b) shows that the metallic states are strongly associated with the surface oxygen orbitals. In summary this gives definitive evidence that the surface states are responsible for the metallic character. Inspection of the bandstructure for the orthogonal wavevector direction  $[110]$  also provides evidence of metallic states. This suggests that the surface conductivity at the (110) surface is essentially isotropic, and metallic conduction in all surface directions should be possible.

The bandstructure for the (001) surface slab is plotted in Figure 6 for the set of wavevectors aligned with the  $[1\bar{1}0]$  direction. The spin up bandstructure in Figure 6a possesses just a single band crossing the Fermi level near the zone center wavevector,  $\Gamma$ . This state does not possess a character strongly associated with surface atoms, but rather is free-electron-like suggesting the presence of states similar to a 2D electron gas. The spin down bandstructure in Figure 6b possesses a more complex dispersion near the Fermi level compared to the (110) surface. Furthermore, the metallic states that cross the Fermi level possess contributions from both surface O and Mn sites. There is a band with especially strong surface oxygen character that crosses the Fermi level approximately halfway to the zone boundary. This is followed by a band of strong surface Mn character crossing the Fermi level nearer the zone boundary. The fact that the projection of each atom type is associated with different bands suggests that the electron hopping will be O to O and Mn to Mn, rather than mixed site Mn to O. It is likely that mixed site hopping will occur instead as a result of scattering, for instance due to impurities or temperature fluctuations. In contrast to the (110) surface, inspection of the (001) bandstructure along the orthogonal  $[001]$  direction indicates gapped states. Consequently, the metallic conductivity at this surface is not isotropic and is likely to be dominated by the  $[1\bar{1}0]$  direction.

It may be suggested that the observed metallic states could be removed by reduction or oxidation of the surface. However, Oxford and Chaka<sup>47</sup> in a recent comprehensive study found the stoichiometric (110) surface to be stable over most of the range

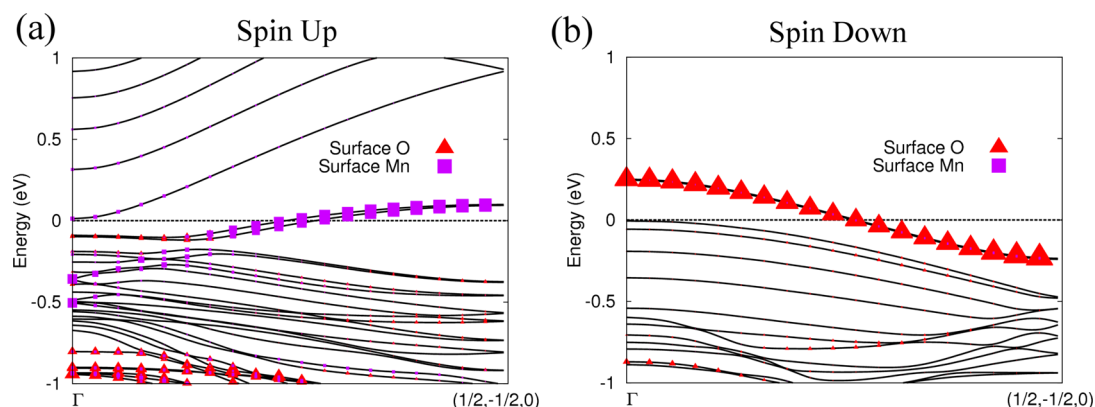


**Figure 5.** Surface band structure for the slab of the (110) surface. The band character of the surface oxygen is shown in red and for surface manganese in purple. The surface oxygen clearly gives the greatest contribution to the metallic bands in the spin down channel.

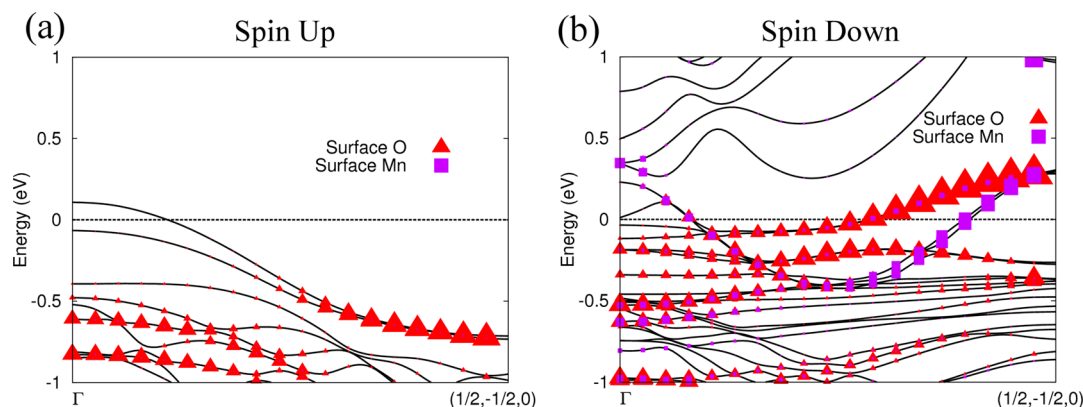


**Figure 6.** Surface band structure for the slab of the (001) surface. The band character of the surface oxygen is shown in red and that for surface manganese is shown in purple. The surface oxygen and manganese both contribute to the metallic bands in the spin down channel.

of experimentally relevant conditions. Furthermore, the small bulk band gap of rutile  $\text{MnO}_2$  suggests that the energy cost for forming metallic states will be low. Therefore, with appropriately directed synthesis there is the potential to express surfaces with advantageous metallicity for the optimization of practical materials. Furthermore, the application of GW or hybrid DFT to this problem would be worthwhile, but because of their large computational expense for surface slabs is left for future work.

## CONCLUSIONS

Density functional theory has been employed to deepen our understanding of the surface electronic structure of rutile  $\text{MnO}_2$ . The primary finding is that the (110) and (001) surfaces possess metallic surface states. These states are shown to be primarily associated with spin-polarized surface oxygen sites and to a lesser degree surface Mn sites. There is a strong connection between the broken coordination due to cleaving the surface and the metallic states. The presence of surface metallicity may aid the supply of electrons to reactions during the catalytic activity of rutile  $\text{MnO}_2$ . Bader charges evidence incomplete Mn–O charge transfer that indicates the surface sites are not purely ionic. Other surfaces, (211) and (311), expressed in the calculated equilibrium morphology are, however, similarly gapped to bulk rutile  $\text{MnO}_2$ . This demonstrates that the presence of surface metallicity is sensitive to the specific surface terminations, not just the nature of the bulk crystal that is cleaved. Furthermore, the metallic states at

the (001) surface are found to be highly anisotropic and give one-dimensional conduction along the  $[1\bar{1}0]$  direction.

In light of recent discoveries of superconductivity and intriguing magnetic phenomena at interfaces, the observed potential to engineer metallic behavior at the surfaces of this insulating oxide may provide a new pathway to explore novel states of matter.

## AUTHOR INFORMATION

### Corresponding Authors

\*E-mail: dt331@bath.ac.uk.

\*E-mail: m.s.islam@bath.ac.uk. Tel.: +44 7907566351, +44(0) 1225 384938. Fax: +44(0)1225 386231.

### Notes

The authors declare no competing financial interest.

## ACKNOWLEDGMENTS

We are grateful to the EPSRC for funding (EP/L000202) and to the Materials Chemistry Consortium for ARCHER super-computer resources.

## REFERENCES

- (1) Hansson, G. V.; Uhrberg, R. I. Photoelectron spectroscopy of surface states on semiconductor surfaces. *Surf. Sci. Rep.* **1988**, *9*, 197–292.
- (2) Kubby, J.; Boland, J. Scanning tunneling microscopy of semiconductor surfaces. *Surf. Sci. Rep.* **1996**, *26*, 61–204.

- (3) Hwang, H. Y.; Iwasa, Y.; Kawasaki, M.; Keimer, B.; Nagaosa, N.; Tokura, Y. Emergent phenomena at oxide interfaces. *Nat. Mater.* **2012**, *11*, 103–113.
- (4) Jiao, F.; Bruce, P. G. Mesoporous crystalline  $\beta$ - $\text{MnO}_2$ —a reversible positive electrode for rechargeable lithium batteries. *Adv. Mater.* **2007**, *19*, 657–660.
- (5) Luo, J.-Y.; Zhang, J.-J.; Xia, Y.-Y. Highly electrochemical reaction of lithium in the ordered mesoporous  $\beta$ - $\text{MnO}_2$ . *Chem. Mater.* **2006**, *18*, 5618–5623.
- (6) Mathew, V.; Lim, J.; Kang, J.; Gim, J.; Rai, A. K.; Kim, J. Self-assembled mesoporous manganese oxide with high surface area by ambient temperature synthesis and its enhanced electrochemical properties. *Electrochem. Commun.* **2011**, *13*, 730–733.
- (7) Cheng, F.; Zhao, J.; Song, W.; Li, C.; Ma, H.; Chen, J.; Shen, P. Facile controlled synthesis of  $\text{MnO}_2$  nanostructures of novel shapes and their application in batteries. *Inorg. Chem.* **2006**, *45*, 2038–2044.
- (8) Tang, W.; Yang, X.; Liu, Z.; Ooi, K. Preparation of  $\beta$ - $\text{MnO}_2$  nanocrystal/acetylene black composites for lithium batteries. *J. Mater. Chem.* **2003**, *13*, 2989–2995.
- (9) Lang, X.; Hirata, A.; Fujita, T.; Chen, M. Nanoporous metal/oxide hybrid electrodes for electrochemical supercapacitors. *Nat. Nanotechnol.* **2011**, *6*, 232–236.
- (10) Subramanian, V.; Zhu, H.; Vajtai, R.; Ajayan, P. M.; Wei, B. Hydrothermal synthesis and pseudocapacitance properties of  $\text{MnO}_2$  nanostructures. *J. Phys. Chem. B* **2005**, *109*, 20207–20214.
- (11) Devaraj, S.; Munichandraiah, N. Effect of crystallographic structure of  $\text{MnO}_2$  on its electrochemical capacitance properties. *J. Phys. Chem. C* **2008**, *112*, 4406–4417.
- (12) Zang, J.; Li, X. In situ synthesis of ultrafine  $\beta$ - $\text{MnO}_2$ /polypyrrole nanorod composites for high-performance supercapacitors. *J. Mater. Chem.* **2011**, *21*, 10965–10969.
- (13) Debart, A.; Paterson, A. J.; Bao, J.; Bruce, P. G.  $\alpha$ - $\text{MnO}_2$  nanowires: A catalyst for the  $\text{O}_2$  electrode in rechargeable lithium batteries. *Angew. Chem., Int. Ed.* **2008**, *47*, 4521–4524.
- (14) Thapa, A. K.; Hidaka, Y.; Hagiwara, H.; Ida, S.; Ishihara, T. Mesoporous  $\beta$ - $\text{MnO}_2$  air electrode modified with Pd for rechargeability in lithium–air battery. *J. Electrochem. Soc.* **2011**, *158*, A1483–A1489.
- (15) Zhou, F.; Kang, K.; Maxisch, T.; Ceder, G.; Morgan, D. The electronic structure and band gap of  $\text{LiFePO}_4$  and  $\text{LiMnPO}_4$ . *Solid State Commun.* **2004**, *132*, 181–186.
- (16) Goodenough, J. B.; Kim, Y. Challenges for rechargeable Li batteries. *Chem. Mater.* **2010**, *22*, 587–603.
- (17) Janssen, Y.; Middlemiss, D. S.; Bo, S.-H.; Grey, C. P.; Khalifah, P. G. Structural modulation in the high capacity battery cathode material  $\text{LiFeBO}_3$ . *J. Am. Chem. Soc.* **2012**, *134*, 12516–12527.
- (18) Tompsett, D. A.; Middlemiss, D. S.; Islam, M. S. Importance of anisotropic Coulomb interactions and exchange to the band gap and antiferromagnetism of  $\beta$ - $\text{MnO}_2$  from DFT+U. *Phys. Rev. B* **2012**, *86*, 205126.
- (19) Reddy, A. L. M.; Shaijumon, M. M.; Gowda, S. R.; Ajayan, P. M. Coaxial  $\text{MnO}_2$ /carbon nanotube array electrodes for high-performance lithium batteries. *Nano Lett.* **2009**, *9*, 1002–1006.
- (20) Liu, R.; Duay, J.; Lee, S. B. Heterogeneous nanostructured electrode materials for electrochemical energy storage. *Chem. Commun.* **2011**, *47*, 1384–1404.
- (21) Bewlay, S.; Konstantinov, K.; Wang, G.; Dou, S.; Liu, H. Conductivity improvements to spray-produced  $\text{LiFePO}_4$  by addition of a carbon source. *Mater. Lett.* **2004**, *58*, 1788–1791.
- (22) Kijima, N.; Sakata, Y.; Takahashi, Y.; Akimoto, J.; Kumagai, T.; Igarashi, K.; Shimizu, T. Synthesis and lithium ion insertion/extraction properties of hollandite-type  $\text{MnO}_2$  prepared by acid digestion of  $\text{Mn}_2\text{O}_3$ . *Solid State Ionics* **2009**, *180*, 616–620.
- (23) Thackeray, M. Manganese oxides for lithium batteries. *Prog. Solid State Chem.* **1997**, *25*, 1–71.
- (24) Tompsett, D. A.; Islam, M. S. Electrochemistry of hollandite  $\alpha$ - $\text{MnO}_2$ : Li-ion and Na-ion insertion and  $\text{Li}_2\text{O}$  incorporation. *Chem. Mater.* **2013**, *25*, 2515–2526.
- (25) Roche, I.; Chainet, E.; Chatenet, M.; Vondrak, J. Carbon-supported manganese oxide nanoparticles as electrocatalysts for the oxygen reduction reaction (ORR) in alkaline medium: Physical characterizations and ORR mechanism. *J. Phys. Chem. C* **2007**, *111*, 1434–1443.
- (26) Eary, L.; Rai, D. Kinetics of chromium(III) oxidation to chromium(VI) by reaction with manganese-dioxide. *Environ. Sci. Technol.* **1987**, *21*, 1187–1193.
- (27) Weaver, R.; Hochella, M.; Ilton, E. Dynamic processes occurring at the Cr-aq(III)–Manganite ( $\gamma$ - $\text{MnOOH}$ ) interface: Simultaneous adsorption, microprecipitation, oxidation/reduction, and dissolution. *Geochim. Cosmochim. Acta* **2002**, *66*, 4119–4132.
- (28) Nesbitt, H.; Canning, G.; Bancroft, G. XPS study of reductive dissolution of 7 angstrom-birnessite by  $\text{H}_3\text{AsO}_3$ , with constraints on reaction mechanism. *Geochim. Cosmochim. Acta* **1998**, *62*, 2097–2110.
- (29) Zhu, M.; Paul, K. W.; Kubicki, J. D.; Sparks, D. L. Quantum chemical study of arsenic (III, V) adsorption on Mn-oxides: Implications for arsenic(III) oxidation. *Environ. Sci. Technol.* **2009**, *43*, 6655–6661.
- (30) El-Deab, M. S.; Awad, M. I.; Mohammad, A. M.; Ohsaka, T. Enhanced water electrolysis: Electrocatalytic generation of oxygen gas at manganese oxide nanorods modified electrodes. *Electrochem. Commun.* **2007**, *9*, 2082–2087.
- (31) Freunberger, S. A.; Chen, Y.; Peng, Z.; Griffin, J. M.; Hardwick, L. J.; Barde, F.; Novak, P.; Bruce, P. G. Reactions in the rechargeable lithium- $\text{O}_2$  battery with alkyl carbonate electrolytes. *J. Am. Chem. Soc.* **2011**, *133*, 8040–8047.
- (32) Xiao, J.; Hu, J.; Wang, D.; Hu, D.; Xu, W.; Graff, G. L.; Nie, Z.; Liu, J.; Zhang, J.-G. Investigation of the rechargeability of Li- $\text{O}_2$  batteries in non-aqueous electrolyte. *J. Power Sources* **2011**, *196*, 5674–5678.
- (33) Xu, W.; Viswanathan, V. V.; Wang, D.; Towne, S. A.; Xiao, J.; Nie, Z.; Hu, D.; Zhang, J.-G. Investigation on the charging process of  $\text{Li}_2\text{O}_2$ -based air electrodes in Li- $\text{O}_2$  batteries with organic carbonate electrolytes. *J. Power Sources* **2011**, *196*, 3894–3899.
- (34) Mizuno, F.; Nakanishi, S.; Kotani, Y.; Yokoishi, S.; Iba, H. Rechargeable Li–air batteries with carbonate-based liquid electrolytes. *Electrochemistry* **2010**, *78*, 403–405 50th Battery Symposium in Japan, Kyoto, Japan, Nov 30-Dec 02, 2009.
- (35) Jung, H.-G.; Hassoun, J.; Park, J.-B.; Sun, Y.-K.; Scrosati, B. An improved high-performance lithium–air battery. *Nat. Chem.* **2012**, *4*, 579–585.
- (36) Peng, Z.; Freunberger, S. A.; Chen, Y.; Bruce, P. G. A reversible and higher-rate Li- $\text{O}_2$  battery. *Science* **2012**, *337*, 563–566.
- (37) Tompsett, D. A.; Parker, S. C.; Islam, M. S. Rutile  $\beta$ - $\text{MnO}_2$  surfaces and vacancy formation for high electrochemical and catalytic performance. *J. Am. Chem. Soc.* **2014**, *136*, 1418–1426.
- (38) Zhang, H.; Cao, G.; Wang, Z.; Yang, Y.; Shi, Z.; Gu, Z. Growth of manganese oxide nanoflowers on vertically-aligned carbon nanotube arrays for high-rate electrochemical capacitive energy storage. *Nano Lett.* **2008**, *8*, 2664–2668.
- (39) Tompsett, D. A.; Parker, S. C.; Bruce, P. G.; Islam, M. S. Nanostructuring of  $\beta$ - $\text{MnO}_2$ : The important role of surface to bulk ion migration. *Chem. Mater.* **2013**, *25*, 536–541.
- (40) Wolf, S. A.; Awschalom, D. D.; Buhrman, R. A.; Daughton, J. M.; von Molnár, S.; Roukes, M. L.; Chtchelkanova, A. Y.; Treger, D. M. Spintronics: A spin-based electronics vision for the future. *Science* **2001**, *294*, 1488–1495.
- (41) Baur, W. Rutile-type compounds 5. Refinement of  $\text{MnO}_2$  and  $\text{MgF}_2$ . *Acta Crystallogr. B* **1976**, *32*, 2200–2204.
- (42) Regulski, M.; Przeniosło, R.; Sosnowska, I.; Hoffmann, J.-U. Short and long range magnetic ordering in  $\beta$ - $\text{MnO}_2$ . *J. Phys. Soc. Jpn.* **2004**, *73*, 3444–3447.
- (43) Oku, M.; Hirokawa, K.; Ikeda, S. X-ray photoelectron spectroscopy of manganese–oxygen systems. *J. Electron Spectrosc.* **1975**, *7*, 465–473.
- (44) Chambers, S.; Liang, Y. Growth of  $\beta$ - $\text{MnO}_2$  films on  $\text{TiO}_2(110)$  by oxygen plasma assisted molecular beam epitaxy. *Surf. Sci.* **1999**, *420*, 123–133.

(45) Xing, X. J.; Yu, Y. P.; Xu, L. M.; Wu, S. X.; Li, S. W. Magnetic properties of  $\beta$ -MnO<sub>2</sub> thin films grown by plasma-assisted molecular beam epitaxy. *J. Phys. Chem. C* **2008**, *112*, 15526–15531.

(46) Maphanga, R.; Parker, S.; Ngoepe, P. Atomistic simulation of the surface structure of electrolytic manganese dioxide. *Surf. Sci.* **2009**, *603*, 3184–3190.

(47) Oxford, G. A. E.; Chaka, A. M. First-principles calculations of clean, oxidized, and reduced  $\beta$ -MnO<sub>2</sub> surfaces. *J. Phys. Chem. C* **2011**, *115*, 16992–17008.

(48) Oxford, G. A. E.; Chaka, A. M. Structure and stability of hydrated  $\beta$ -MnO<sub>2</sub> surfaces. *J. Phys. Chem. C* **2012**, *116*, 11589–11605.

(49) Li, L.; Wei, Z.; Chen, S.; Qi, X.; Ding, W.; Xia, M.; Li, R.; Xiong, K.; Deng, Z.; Gao, Y. A comparative DFT study of the catalytic activity of MnO<sub>2</sub> (211) and (221) surfaces for an oxygen reduction reaction. *Chem. Phys. Lett.* **2012**, *539–540*, 89–93.

(50) Kresse, G.; Furthmüller, J. Efficient iterative schemes for ab initio total-energy calculations using a plane-wave basis set. *Phys. Rev. B* **1996**, *54*, 11169–11186.

(51) Perdew, J.; Burke, K.; Ernzerhof, M. Generalized gradient approximation made simple. *Phys. Rev. Lett.* **1996**, *77*, 3865–3868.

(52) Anisimov, V. I.; Gunnarsson, O. Density-functional calculation of effective Coulomb interactions in metals. *Phys. Rev. B* **1991**, *43*, 7570–7574.

(53) Madsen, G.; Novak, P. Charge order in magnetite. An LDA+U study. *Europhys. Lett.* **2005**, *69*, 777–783.

(54) Schwarz, K.; Blaha, P. Solid state calculations using WIEN2k. *Comput. Mater. Sci.* **2003**, *28*, 259–273.

(55) Antonides, E.; Janse, E. C.; Sawatzky, G. A. LMM Auger spectra of Cu, Zn, Ga, and Ge. I. Transition probabilities, term splittings, and effective Coulomb interaction. *Phys. Rev. B* **1977**, *15*, 1669–1679.

(56) Anisimov, V. I.; Zaanen, J.; Andersen, O. K. Band theory and Mott insulators: Hubbard U instead of Stoner I. *Phys. Rev. B* **1991**, *44*, 943–954.

(57) Ylvisaker, E. R.; Pickett, W. E.; Koepfner, K. Anisotropy and magnetism in the LSDA + U method. *Phys. Rev. B* **2009**, *79*, 035103.

(58) Morgan, B. J.; Watson, G. W. A density functional theory plus U study of oxygen vacancy formation at the (110), (100), (101), and (001) surfaces of rutile TiO<sub>2</sub>. *J. Phys. Chem. C* **2009**, *113*, 7322–7328.

(59) Henrich, V. E.; Kurtz, R. L. Surface electronic structure of TiO<sub>2</sub>: Atomic geometry, ligand coordination, and the effect of adsorbed hydrogen. *Phys. Rev. B* **1981**, *23*, 6280–6287.

(60) Radin, M. D.; Rodriguez, J. F.; Tian, F.; Siegel, D. J. Lithium peroxide surfaces are metallic, while lithium oxide surfaces are not. *J. Am. Chem. Soc.* **2012**, *134*, 1093–1103.

(61) Eriksson, T.; Gustafsson, T.; Thomas, J. O. Surface structure of LiMn<sub>2</sub>O<sub>4</sub> electrodes. *Electrochem. Solid-State Lett.* **2002**, *5*, A35–A38.